LETTER

doi:10.1038/nature24043

Structural phase transition in monolayer $MoTe_2$ driven by electrostatic doping

Ying Wang[1]*, Jun Xiao[1]*, Hanyu Zhu[1], Yao Li[2], Yousif Alsaid[1], King Yan Fong[1], Yao Zhou[2], Siqi Wang[1], Wu Shi[3,4], Yuan Wang[1], Alex Zettl[3,4], Evan J. Reed[2] & Xiang Zhang[1,3,5]

Monolayers of transition-metal dichalcogenides (TMDs) exhibit numerous crystal phases with distinct structures, symmetries and physical properties[1–3]. Exploring the physics of transitions between these different structural phases in two dimensions[4] may provide a means of switching material properties, with implications for potential applications. Structural phase transitions in TMDs have so far been induced by thermal or chemical means[5,6]; purely electrostatic control over crystal phases through electrostatic doping was recently proposed as a theoretical possibility, but has not yet been realized[7,8]. Here we report the experimental demonstration of an electrostatic-doping-driven phase transition between the hexagonal and monoclinic phases of monolayer molybdenum ditelluride ($MoTe_2$). We find that the phase transition shows a hysteretic loop in Raman spectra, and can be reversed by increasing or decreasing the gate voltage. We also combine second-harmonic generation spectroscopy with polarization-resolved Raman spectroscopy to show that the induced monoclinic phase preserves the crystal orientation of the original hexagonal phase. Moreover, this structural phase transition occurs simultaneously across the whole sample. This electrostatic-doping control of structural phase transition opens up new possibilities for developing phase-change devices based on atomically thin membranes.

The crystal form commonly studied among layered TMDs is the most stable hexagonal (2H) phase. In this case, as shown in Fig. 1a, each monolayer is composed of a layer of hexagonally arranged transition-metal atoms, sandwiched between two layers of chalcogen atoms[1]. Unlike the bulk form, monolayer 2H TMDs become direct-bandgap semiconductors and break inversion symmetry, creating inequivalent valleys at the corners of the Brillouin zone[9,10]. This valley degree of freedom, together with the strong excitonic effect in low dimensions, makes this phase a unique platform for two-dimensional valleytronics and optoelectronics[11–13]. Intriguingly, experimental studies have reported another layered crystal structure, namely the monoclinic (1T′) phase. Here, in each layer chalcogen atoms form an octahedral coordination around transition-metal atoms, with a lattice distortion along the *y*-axis[14] (Fig. 1b). Unlike the semiconducting 2H phase, the semimetallic or metallic 1T′ monolayer TMDs retain inversion symmetry and are predicted to exhibit non-trivial topological states[2,3]. The dynamic control of transitions between the 2H and 1T′ phases can reveal the competition, coexistence and cooperation of different crystal structures, as well as interplay among distinct physical properties[15]. Such control also leads to broad device applications such as memory devices, reconfigurable circuits and topological transistors at atomically thin limits[2,16,17].

So far, the 2H-to-1T′ phase change in TMDs such as $MoTe_2$ has been experimentally reported through thermal synthesis at 500 °C (ref. 5), irreversible growth by element substitution[18], and laser irradiation[19]. However, these phase transitions were only found in a few layers or in the bulk sample, and have not yet been realized in monolayers. Reaching the two-dimensional limit is important for exploring phase-ordering competition that involves largely enhanced electron–phonon and electron–electron interactions, which are the basis of many-body phenomena such as high-temperature superconductivity[20]. It also opens up access to unique properties in monolayer materials such as the valley degree of freedom[9], Ising pairing[21] and topological transport[3].

Electrostatic gating has been proposed as a feasible means of controlling phase transitions in monolayer TMDs[7,8], and is also expected to be dynamic, reversible and free from impurities. This is important for potential applications such as memory switching and reconfigurable devices. This new approach takes advantage of the electrically tunable doping level of up to 10^{14} electrons per square centimetre in ultrathin TMDs[22]. The excessive electrons, injected into a monolayer of the 2H phase under an electrostatic bias, will occupy the lowest available energy states in the conduction band; the energy of these states is hundreds of milli-electron volts higher than that in the 1T′ phase[7]. Therefore, at high doping levels, the extra electrons are expected to carry enough energy to lift the total energy of the 2H phase above that of the 1T′ phase, switching the ground state from 2H to 1T′ and inducing a structural phase transition[7]. Here, we demonstrate such an electrostatically induced structural phase transition between the 2H and 1T′ phases in monolayer $MoTe_2$. We show that this transition occurs uniformly over the whole monolayer, and that the process is reversible and preserves crystal orientation. In addition, the substantial change in crystal symmetry leads to a change in second-harmonic generation (SHG) intensity over one order of magnitude, which can potentially be applied to non-linear electro-optic modulators[23].

The electrostatic-doping-driven structural phase transition from 2H monolayer $MoTe_2$ to the 1T′ phase is realized with an ionic liquid (DEME-TFSI) field-effect transistor (see Fig. 1c, d and Methods), which can reach a doping level that is one order of magnitude higher than that of a solid gate[22]. Given that the phonon vibration modes are distinct in different lattice configurations, we used Raman spectroscopy to characterize the phase evolution of the monolayer $MoTe_2$ when sweeping the gate voltage (Fig. 2a). We specifically chose the excitation wavelength to be 633 nm, which yields a large Raman intensity on monolayers[24], and kept the power under 1 mW μm^{-2}, eliminating the chance of inducing the 1T′ phase or sample damage through laser irradiation[19]. When the top gate is biased to 0 V, the initial exfoliated 2H monolayer $MoTe_2$ shows two characteristic Raman peaks: at 171.5 cm^{-1} (representing the out-of-plane A_1' mode) and 236 cm^{-1} (the in-plane E′ mode). Both peaks display a simultaneous intensity drop and linewidth broadening when the gate bias is higher than 2.8 V—one signature of ongoing bond breaking and disappearance of the 2H phase. Meanwhile, Raman spectra also exhibit a rising new peak at 167.5 cm^{-1}. By verifying that these measured Raman spectra are consistent with

[1]NSF Nanoscale Science and Engineering Center (NSEC), 3112 Etcheverry Hall, University of California, Berkeley, California 94720, USA. [2]Department of Materials Science and Engineering, Stanford University, Stanford, California 94305, USA. [3]Materials Sciences Division, Lawrence Berkeley National Laboratory, 1 Cyclotron Road, Berkeley, California 94720, USA. [4]Kavli Energy NanoSciences Institute and Department of Physics, University of California, Berkeley, California 94720, USA. [5]Department of Physics, King Abdulaziz University, Jeddah 21589, Saudi Arabia.
*These authors contributed equally to this work.

© 2017 Macmillan Publishers Limited, part of Springer Nature. All rights reserved.

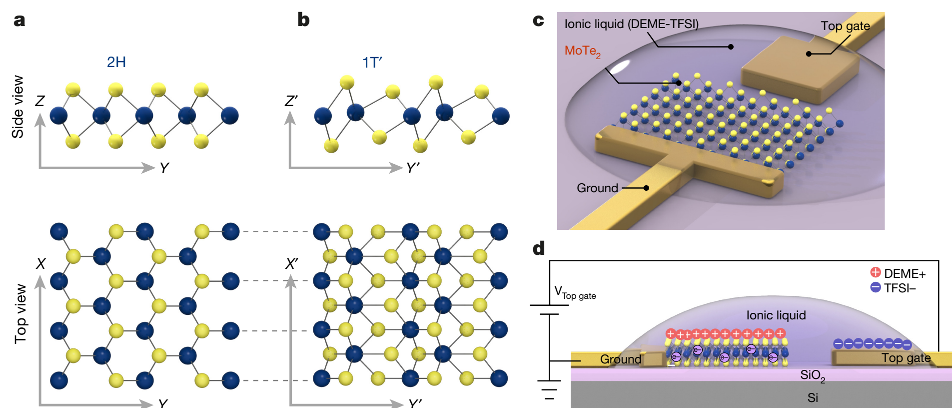

Figure 1 | Electrostatic-doping-driven structural phase transition in a gating device. a, **b**, Crystal structures of the 2H (**a**) and 1T′ (**b**) phases of monolayer TMDs. Blue spheres, metal atoms (molybdenum or tungsten); yellow spheres, chalcogens (selenium, sulfur or tellurium). In our experiment, the coloured spheres represent molybdenum and tellurium atoms. The 2H phase has a trigonal prismatic structure and lacks inversion symmetry; the 1T′ phase has a distorted octahedral structure and inversion symmetry. **c**, **d**, Schematics and measurement configuration of a $MoTe_2$ monolayer field-effect transistor. A monolayer of $MoTe_2$ is exfoliated onto a silicon wafer covered with a silicon oxide layer. The $MoTe_2$ monolayer is anchored by a ground indium/gold electrode; an isolated indium/gold pad nearby is the top-gate electrode, controlling the gate bias. A drop of ionic liquid (*N*,*N*-diethyl-*N*-(2-methoxyethyl)-*N*-methylammonium bis(trifluoromethylsulphonyl-imide), DEME-TFSI) covers the monolayer and the electrodes. This ionic liquid can manipulate the electron population in $MoTe_2$, resulting in a structural transition between the 2H and 1T′ phases. All devices were measured in vacuum and at 220 K.

calculated and measured spectra of pristine monolayer 1T′ $MoTe_2$ (Extended Data Figs 1, 2), we confirm that this new peak corresponds to the characteristic A_g mode of the 1T′ phase. This evidence clearly points to the formation of the 1T′ phase under gate control.

As well as undergoing a change in phonon modes, the structural transition of a crystal is typically accompanied by hysteresis of the relative Raman scattering strength[25]. In our study, we observe and interpret such hysteresis through the ratio of the Raman intensity of the 1T′ phase to the intensity over both phases[26]: $F = 1T'(A_g)/(2H(A_1') + 1T'(A_g))$. To extract separate Raman components of the 1T′ and 2H phases, we fitted the Raman mixture in the range 160 cm^{-1} to 180 cm^{-1} with a Lorentz model (Extended Data Fig. 3). In Fig. 2b, the gate dependence of *F* is plotted in black and red curves, denoting forward and backward gate sweeps, respectively. Below 2.8 V in the forward sweep, *F* remains around zero, meaning that there is a negligible 1T′ fraction. Here, the 2H phase is still dominant with an almost unchanged Raman shift. When the gate bias is increased continuously, *F* starts to incline sharply and approaches 1 when there is an extra bias of 1 V, revealing a nearly complete transition to the 1T′ phase. When the gate voltage is swept backwards, the sample remains in the 1T′ phase until the bias is tuned down to 2.4 V. The 2H phase begins to reappear from then on, and recovers fully at 1.2 V. The width of this hysteresis loop, in terms of gate voltage, is around 1.8 V.

To confirm this phase transition and hysteresis, we also studied the gate-dependent SHG in monolayer $MoTe_2$. Given that inversion symmetry is present in the 1T′ phase but absent in the 2H phase, SHG spectroscopy can be a very sensitive probe for distinguishing these two phases. Both the transition voltage and the width of the hysteresis loop as measured by SHG spectroscopy are consistent with those extracted from Raman spectroscopy (Extended Data Fig. 4a). This consistency clearly demonstrates that the disappearance of the 2H phase and the appearance of the 1T′ phase occur synchronously during the phase transition.

It is worth noting that we carefully dehydrated the ionic liquid at 100 °C for five hours, and waited for two minutes at each gate voltage to

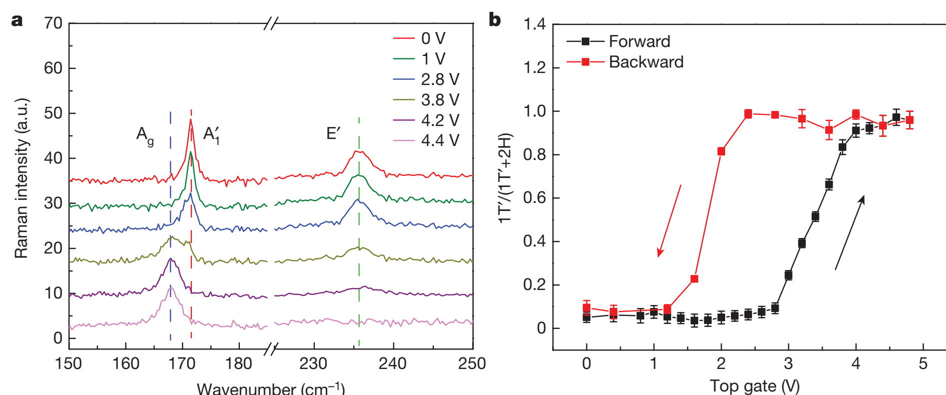

Figure 2 | The 2H-to-1T′ phase transition in monolayer $MoTe_2$ under electrostatic bias. a, Representative Raman spectra before, during and after transition from the 2H to the 1T′ phase, as the bias changes from 0 V to 4.4 V. The characteristic Raman modes of the 2H phase, A_1 and E′ (shown by the red and green dashed lines at 171.5 cm^{-1} and 236 cm^{-1}, respectively) gradually disappear, as the A_g mode of the 1T′ phase appears (167.5 cm^{-1}; blue dashed line). a.u., arbitrary units. **b**, Gate-dependent Raman intensity ratios. The ratio $F = 1T'(A_g)/[2H(A_1') + 1T'(A_g)]$ (*y*-axis) shows hysteresis under an electrical field scan, with a loop width as large as 1.8 V. The black and red curves show increasing and decreasing gate voltage, respectively. The Raman intensity for each mode was extracted from Lorentz fitting of the Raman mixture in the range 160 cm^{-1} to 180 cm^{-1} from Fig. 2a. The error bars represent the standard error propagated from the fitting parameters. The transformation of phonon modes and the corresponding hysteresis loop indicate a clear structural phase transition between 2H and 1T′ phases under gate control.

© 2017 Macmillan Publishers Limited, part of Springer Nature. All rights reserved.

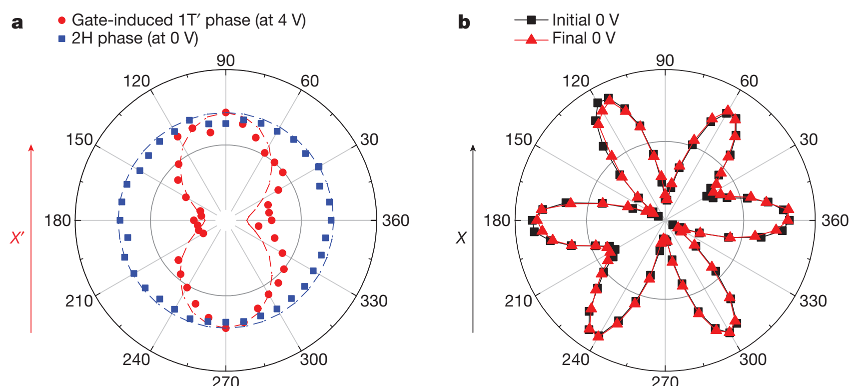

Figure 3 | Preservation of crystal orientation before and after structural transition. a, Raman intensity from monolayer $MoTe_2$ as a function of crystal angle. The polar pattern of the A_1' mode in the 2H phase at 0 V bias (blue squares) is well fitted by a circle (blue dashed line), which shows isotropic Raman scattering. By contrast, the 1T′ phase at 4 V bias exhibits a two-lobe Raman scattering pattern (red dots), agreeing well with our calculation of the anisotropic A_g mode Raman tensor (red dashed line). **b**, SHG intensity from the same monolayer sample as a function of crystal angle. The initial 2H phase at 0 V shows a typical sixfold pattern (black squares connected by a black line). The zigzag direction in the 2H phase (shown as the *X* axis in Fig. 1a) and zigzag direction of distorted molybdenum atoms in the 1T′ phase (shown as the *X*′ axis in Fig. 1b) can be seen to overlap with each other. The sixfold pattern is fully restored in the final 2H phase at 0 V after regrowth from the 1T′ phase (red squares connected by a red line). The overlap and restoration of these crystal axes indicate preservation of crystal orientation through the phase transitions.

allow ions to finish moving. This process largely reduces the loop width of extrinsic hysteresis (which could result from the slow motion of ions or from water contamination in the ionic liquid) down to 0.1 V (ref. 22). In addition, the absence of hysteresis in a bilayer 2H $MoTe_2$ under the same gate-sweeping process further confirms that the observed hysteresis in the monolayer is solely due to the phase transition (Extended Data Fig. 4b). On the basis of the theoretical prediction that the voltage requirement for electrons is less than one half of that for holes, we chose the positive top-gate voltage specifically to induce the phase transition; as expected, no phase transition was observed with a negative gate (Extended Data Fig. 4c).

To understand the microscopic lattice change that occurs during the electrostatic-doping-driven transition, we studied the correlation of bonding orientation between the two phases. In order to compare crystal orientations before and after transition in the same monolayer device, we investigated the polarization dependence of both Raman and SHG spectra. According to symmetry analysis and density functional theory (DFT) calculations, the A_1' mode of 2H-phase $MoTe_2$ has only diagonal components, with identical scattering strength for $A_{1(xx)}'$ and $A_{1(yy)}'$ in the Raman tensor. Meanwhile, the A_g mode of 1T′ phase $MoTe_2$ has scattering anisotropy, with $A_{g(xx)}/A_{g(yy)} = 2.3/1$ (see Methods). This difference results in a circular pattern for the A_1' mode at a gate bias of 0 V, and a two-lobe pattern for the A_g mode at a bias of 4 V, in polarization-resolved Raman measurements (Methods; see Fig. 3a). The two-lobe pattern is also consistent with that of pristine monolayer 1T′ $MoTe_2$ (Extended Data Fig. 5). The axis connecting the Raman scattering maxima in the two lobes lies in the direction of the molybdenum atom along the X′ coordinate (Fig. 1b).

In order to identify the crystal orientation of the 2H phase for the same monolayer sample, we obtained typical measurements of the angular dependence of polarized SHG[27]. As shown in Fig. 3b, monolayer 2H $MoTe_2$ shows a strong SHG signal under a 1,066-nm ultrafast laser pump. Rotating the excitation and detection polarizations co-directionally clearly reveals a sixfold SHG pattern. Intriguingly, we found that the zigzag direction (the *X* coordinate in Fig. 1a) with the minimum SHG intensity in the original 2H phase overlaps with the zigzag chains of distorted molybdenum atoms (along the *X*′ coordinate in Fig. 1b) in the gate-induced 1T′ phase. We found this preservation of crystal orientation before and after the phase transition in multiple samples. This finding indicates that it is energetically favourable for the zigzag axis to be maintained during phase transition through intra-layer atomic plane gliding. This was suggested in a previous study that used scanning transmission electron microscopy[4], but our work shows that such orientation locking occurs on a much larger scale (about 10 μm^2) than was shown before (about 10 nm^2). We also compared the polarized SHG patterns at zero bias before and after a full loop of gate scanning: both the sixfold pattern of the 2H phase and the crystal orientation recover (Fig. 3b). Such reversibility of crystal orientation guarantees predictable crystal evolution under gate operation, and will be important for phase-transition devices with repetitive cycles.

Finally, the gate dependence of spatial SHG mapping shows that this phase-transition process is similar over the entire sample (Fig. 4a). Under 1,066-nm laser excitation, SHG mapping of a monolayer flake without bias (Fig. 4b) shows a slight intensity variation over the flake, which we suspect results from local electron charging[28]. Then, when a forward bias of up to 4 V is applied, a typical gate scan with a fine step is obtained (Fig. 4c). When the gate bias is tuned upwards, the SHG intensity gradually increases, owing to modification of the absorption profile by doping in the 2H phase[23]. Increasing the bias further from 2.2 V to 3.6 V produces a sharp drop in the SHG intensity by more than one order of magnitude. By carefully excluding a doping-induced absorption change in the 2H phase as a major contributing factor (Extended Data Figs 4a, 6), we mainly attribute such a drop to a transition from the 2H phase to the 1T′ phase, which preserves inversion symmetry and prohibits SHG.

This gate-dependent SHG curve is well fitted by the Preisach model (Methods), which suggests that a voltage threshold of around 3 V will induce the phase transition. By applying this type of fitting to the whole flake, we mapped out the spatial distribution of the voltage threshold (Fig. 4d). Except for a few points at the edges, the threshold voltages over the monolayer $MoTe_2$ centre at 3 V, with a small standard deviation of 0.1 V; this finding suggests a near-uniform and global transition, with substantial changes in crystal symmetry, over a scale of tens of micrometres and controlled by electrostatic gating (Extended Data Fig. 7). In addition, measurement of the Hall effect on another device—a typical method of estimating carrier density—indicates the threshold doping level to be $2.2 \times 10^{14}\ cm^{-2}$ (see Methods and Extended Data Fig. 8a, b). This doping level is higher than that predicted theoretically[7] ($0.4–1 \times 10^{14}\ cm^{-2}$). We suspect that the difference results from the presence of kinetic barriers during transition, which is not considered in the theoretical calculation. Such kinetic barriers lead to observable hysteresis and set a requirement for a higher doping level to achieve transition. If we ignore the kinetic barrier, then we determine the

© 2017 Macmillan Publishers Limited, part of Springer Nature. All rights reserved.

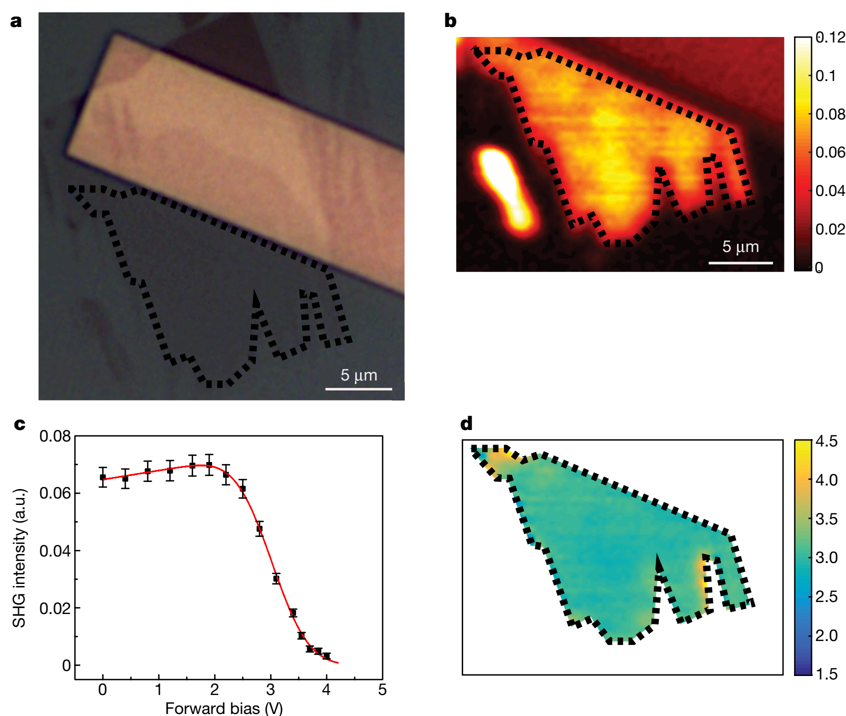

Figure 4 | Spatial mapping of phase transitions in a $MoTe_2$ monolayer by SHG spectroscopy. a, Optical image of a monolayer $MoTe_2$ flake (enclosed by the black dashed line) in contact with an electrode (yellow rectangle). **b**, At zero gate bias, the monolayer (enclosed by the dashed line) shows a strong SHG signal over the whole flake owing to the broken inversion symmetry in the 2H phase. The colour bar indicates the SHG intensity, in arbitrary units. **c**, Typical gate-dependent SHG intensity for this monolayer under forward bias. When the voltage bias is increased from 2 V to 4 V, the SHG intensity shows a sharp decrease to the level of noise. This drop can be attributed mainly to formation of the 1T′ phase, which restores inversion symmetry and prohibits SHG. The SHG trend can be well fitted by the Preisach model (see Methods). The fitting (red curve) suggests a voltage threshold of around 3 V for the induced phase transition. The error bars represent the standard error calculated from the fluctuation of the signal and the digital noise. **d**, Spatial distribution of the voltage threshold obtained by fitting in the Preisach model. For the target monolayer, the voltage thresholds centre at 3 V with a standard deviation of 0.1 V across the two-dimensional crystal, indicating a near-uniform and global structural phase transition. The colour bar indicates the voltage threshold (in volts).

critical voltage—at which the two phases are energy-degenerate—to be 2.4 V with an uncertainty of ± 0.1 V (see Methods). The carrier density at such a voltage range is $0.85 \times 10^{14} \pm 0.16 \times 10^{14}\,\mathrm{cm}^{-2}$ (Methods), which is consistent with the theoretical prediction. Further experiments exclude the laser-induced thermal or strain effect as transition mechanisms in our system (Extended Data Fig. 9).

The phase transition observed here is purely structural, occurring between two different crystal groups (2H and 1T′) and involving large atomic displacements and bond reconstruction. Meanwhile, the final state in our system is determined purely by the gate doping; in this way, reversible and dynamic phase transition is possible at a fixed temperature. Our findings differ from recent reports showing the modification through gate doping of a thermally driven charge density wave (CDW) in a few layers of 1T phase tantalum sufide[29,30] and 1T phase titanium diselenide[31], and from a study that used an in-plane current to trigger a transition from a nearly commensurate CDW state to a commensurate CDW state in 1T phase tantalum sulfide[32,33]. In the latter case, the in-plane current helped a metastable state to overcome transition barriers, and the system finally stabilized at ground state, determined by the temperature rather than by the current. These CDW phase transitions are predominantly electronic, accompanied by some minor lattice distortion. In particular, the sharp jump in temperature-dependent electrical resistance results from Mott physics, where strong electron correlation induces a bandgap at the Fermi level.

In conclusion, we have demonstrated reversible electrical manipulation of a structural phase transition in monolayer $MoTe_2$. Our method for controlling this phase transition provides a versatile platform for studying the fundamental physics of ordering competition and novel topological phases. In addition, the observed large hysteresis and modulation depth will aid the development of two-dimensional memory and reconfigurable devices.

Online Content Methods, along with any additional Extended Data display items and Source Data, are available in the online version of the paper; references unique to these sections appear only in the online paper.

Received 5 December 2016; accepted 10 August 2017.
Published online 11 October 2017.

1. Mak, K. F., Lee, C., Hone, J., Shan, J. & Heinz, T. F. Atomically thin MoS_2: a new direct-gap semiconductor. *Phys. Rev. Lett.* **105,** 136805 (2010).
2. Qian, X., Liu, J., Fu, L. & Li, J. Quantum spin Hall effect in two-dimensional transition metal dichalcogenides. *Science* **346,** 1344–1347 (2014).
3. Ma, Y. *et al.* Quantum spin Hall effect and topological phase transition in two-dimensional square transition-metal dichalcogenides. *Phys. Rev. B* **92,** 085427 (2015).
4. Lin, Y.-C., Dumcenco, D. O., Huang, Y.-S. & Suenaga, K. Atomic mechanism of phase transition between metallic and semiconducting MoS_2 single-layers. *Nat. Nanotechnol.* **9,** 391–396 (2014).
5. Keum, D. H. *et al.* Bandgap opening in few-layered monoclinic $MoTe_2$. *Nat. Phys.* **11,** 482–486 (2015).
6. Kappera, R. *et al.* Phase-engineered low-resistance contacts for ultrathin MoS_2 transistors. *Nat. Mater.* **13,** 1128–1134 (2014).
7. Li, Y., Duerloo, K.-A. N., Wauson, K. & Reed, E. J. Structural semiconductor-to-semimetal phase transition in two-dimensional materials induced by electrostatic gating. *Nat. Commun.* **7,** 10671 (2016).
8. Zhang, C. *et al.* Charge mediated reversible metal-insulator transition in monolayer $MoTe_2$ and $W_xMo_{1-x}Te_2$ alloy. *ACS Nano* **10,** 7370–7375 (2016).

© 2017 Macmillan Publishers Limited, part of Springer Nature. All rights reserved.

9. Wang, Q. H., Kalantar-Zadeh, K., Kis, A., Coleman, J. N. & Strano, M. S. Electronics and optoelectronics of two-dimensional transition metal dichalcogenides. *Nat. Nanotechnol.* **7,** 699–712 (2012).
10. Xiao, D., Liu, G.-B., Feng, W., Xu, X. & Yao, W. Coupled spin and valley physics in monolayers of MoS_2 and other group-VI dichalcogenides. *Phys. Rev. Lett.* **108,** 196802 (2012).
11. Cao, T. *et al.* Valley-selective circular dichroism of monolayer molybdenum disulphide. *Nat. Commun.* **3,** 887 (2012).
12. Mak, K. F., McGill, K. L., Park, J. & McEuen, P. L. The valley Hall effect in MoS_2 transistors. *Science* **344,** 1489–1492 (2014).
13. Ye, Z. *et al.* Probing excitonic dark states in single-layer tungsten disulfide. *Nature* **513,** 214–218 (2014).
14. Wilson, J. A. & Yoffe, A. D. The transition metal dichalcogenides discussion and interpretation of the observed optical, electrical and structural properties. *Adv. Phys.* **18,** 193–335 (1969).
15. Imada, M., Fujimori, A. & Tokura, Y. Metal-insulator transitions. *Rev. Mod. Phys.* **70,** 1039–1263 (1998).
16. Wang, Q. *et al.* Optically reconfigurable metasurfaces and photonic devices based on phase change materials. *Nat. Photon.* **10,** 60–65 (2016).
17. Wuttig, M. & Yamada, N. Phase-change materials for rewriteable data storage. *Nat. Mater.* **6,** 824–832 (2007).
18. Rhodes, D. *et al.* Engineering the structural and electronic phases of $MoTe_2$ through W substitution. *Nano Lett.* **17,** 1616–1622 (2017).
19. Cho, S. *et al.* Phase patterning for ohmic homojunction contact in $MoTe_2$. *Science* **349,** 625–628 (2015).
20. Ge, J.-F. *et al.* Superconductivity above 100 K in single-layer FeSe films on doped $SrTiO_3$. *Nat. Mater.* **14,** 285–289 (2014).
21. Xi, X. *et al.* Ising pairing in superconducting $NbSe_2$ atomic layers. *Nat. Phys.* **12,** 139–143 (2016).
22. Ye, J. T. *et al.* Superconducting dome in a gate-tuned band insulator. *Science* **338,** 1193–1196 (2012).
23. Seyler, K. L. *et al.* Electrical control of second-harmonic generation in a WSe_2 monolayer transistor. *Nat. Nanotechnol.* **10,** 407–411 (2015).
24. Ruppert, C., Aslan, O. B. & Heinz, T. F. Optical properties and band gap of single- and few-layer $MoTe_2$ crystals. *Nano Lett.* **14,** 6231–6236 (2014).
25. Petrov, G. I., Yakovlev, V. V. & Squier, J. Raman microscopy analysis of phase transformation mechanisms in vanadium dioxide. *Appl. Phys. Lett.* **81,** 1023–1025 (2002).
26. Colomban, P. & Slodczyk, A. Raman intensity: an important tool to study the structure and phase transitions of amorphous/crystalline materials. *Opt. Mater.* **31,** 1759–1763 (2009).
27. Li, Y. *et al.* Probing symmetry properties of few-layer MoS2 and h-BN by optical second-harmonic generation. *Nano Lett.* **13,** 3329–3333 (2013).
28. Sercombe, D. *et al.* Optical investigation of the natural electron doping in thin MoS_2 films deposited on dielectric substrates. *Sci. Rep.* **3,** 3489 (2013).
29. Yu, Y. *et al.* Gate-tunable phase transitions in thin flakes of 1T-TaS_2. *Nat Nanotechnol.* **10,** 270–276 (2015).
30. Yoshida, M. *et al.* Controlling charge-density-wave states in nano-thick crystals of 1T-TaS2. *Sci. Rep.* **4,** 7302 (2014).
31. Li, L. J. *et al.* Controlling many-body states by the electric-field effect in a two-dimensional material. *Nature* **529,** 185–189 (2016).
32. Tsen, A. W. *et al.* Structure and control of charge density waves in two-dimensional 1T-TaS_2. *Proc. Natl Acad. Sci. USA* **112,** 15054–15059 (2015).
33. Yoshida, M., Suzuki, R., Zhang, Y., Nakano, M. & Iwasa, Y. Memristive phase switching in two-dimensional crystals. *Sci. Adv.* **1,** e1500606 (2015).

Acknowledgements We thank S. Zhou, K. Deng and W. Yang from Tsinghua University for providing a 1T′ $MoTe_2$ crystal for reference. This work was supported in part by the Director, Office of Science, Office of Basic Energy Sciences, Materials Sciences and Engineering Division, of the US Department of Energy under contract no. DE-AC02-05CH11231, within the ‘Light-Material Interactions in Energy Conversion’ Energy Frontier Research Center (for optical measurements); under the ‘van der Waals Heterostructures Program’ (for transport studies); and by the National Science Foundation (NSF) under grant EFMA-154274 (for device design and fabrication). Y.L., Y.Z., and E.J.R. acknowledge support from the Army Research Office (grant W911NF-15-1-0570); the Office of Naval Research (grant N00014-15-1-2697); the NSF (grants DMR-1455050 and EECS-1436626); and from the Stanford Graduate Fellowship programme.

Author Contributions Ying W., J.X. and X.Z. initiated the research and designed the experiments; Ying W., J.X. and H.Z. performed Raman measurements; J.X. and Ying W. conducted gate-dependent SHG spectroscopy and mapping; Y.A. and J.X. prepared monolayer $MoTe_2$; and Ying W. fabricated and characterized devices. Ying W. measured the doping level with assistance from K.Y.F., S.W. and W.S. (W.S. was under the guidance of A.Z); Y.L. and Y.Z. performed theoretical calculations under the guidance of E.J.R.; Ying W., J.X., H.Z., Y.Z, W.S., Yuan W., E.J.R. and X.Z. analysed data; Ying W., J.X., H.Z., Y.Z., Yuan W., E.J.R. and X.Z. wrote the manuscript. X.Z. and Yuan W. guided the work.

Author Information Reprints and permissions information is available at www.nature.com/reprints. The authors declare no competing financial interests. Readers are welcome to comment on the online version of the paper. Publisher’s note: Springer Nature remains neutral with regard to jurisdictional claims in published maps and institutional affiliations. Correspondence and requests for materials should be addressed to X.Z. (xiang@berkeley.edu).

Reviewer Information *Nature* thanks A. Castro Neto, Y. Iwasa and R. Simpson for their contribution to the peer review of this work.

© 2017 Macmillan Publishers Limited, part of Springer Nature. All rights reserved.

METHODS

Device fabrication. We obtained 2H phase $MoTe_2$ monolayers by mechanically exfoliating bulky single crystals onto a silicon wafer covered with a 285-nm-thick thermally grown silicon oxide layer. We used Raman spectroscopy and optical contrast to characterize the thickness of the samples[24]. After identifying the positions of monolayers, we patterned electrodes by standard electron-beam lithography, and deposited an electrode metal of indium (5 nm) and gold (100 nm) through thermal evaporation. A drop of ionic liquid (DEME-TFSI) was cast on the top of device, covering both monolayer flakes and the metal pad for gating. After being loaded into the cryostat with high vacuum (2×10^{-6} torr), the whole device was baked at 375 K for hours to drive out residual water from the electrolyte.
Gate-dependent Raman spectroscopy. Raman spectroscopy was performed using a commercial Raman system (Horiba Labram HR Evolution) under normal incidence of a helium-neon laser ($\lambda = 632.8$ nm). The laser beam was focused on the samples by a $\times 50$ objective (numerical aperture 0.6); the beam diameter was about 1 μm. The sample was located in a continuous-flow liquid-nitrogen cryostat. In order to obtain a large enough voltage without involving an electrochemical reaction between the ionic liquid and the $MoTe_2$, all experiments were done at 220 K and the top-gate voltage was kept below 4.5 V (ref. 34). A polarized Raman measurement was achieved by using a visible half-wave plate mounted on a motorized stage before the objective. The incident polarization of the linear polarized laser can be accurately controlled by rotating the half-wave plate. The Raman signal was collected in reflected configuration without an extra polarizer.
Gate-dependent SHG spectroscopy. The excitation light was extracted using an optical parametric oscillator (Inspire HF 100, Spectra Physics, Santa Clara, USA) pumped by a mode-locked titanium-sapphire oscillator. The laser pulse width was approximately 200 fs, and the repetition rate was 80 MHz. The excitation laser was linearly polarized by a 900–1,300 nm polarizing beamsplitter. We can change the polarization of the transmitted p-polarized laser light by rotating an infrared (IR) half-wave plate before pumping the sample. The laser was focused with a $\times 50$ near-IR (NIR) objective on sample located in a continuous-flow liquid-nitrogen cryostat. The SHG signal was detected in the backscattering configuration, analysed by a visible-range polarizer, and finally collected by a cooled charge-coupled device (CCD) spectrometer. In our study of SHG polarization patterns, the half-waveplate and polarizer were rotating co-directionally to keep the detecting polarization of SHG collinear with the polarization of incident light. The transmissivity of the optical system was carefully calibrated to evaluate the absolute power level at the focusing plane. For SHG spatial mapping, a microscope objective (Zeiss $\times 50$; numerical aperture 0.55) was mounted on a three-dimensional piezostage. The excitation and collection light-spot position at the sample plane was scanned by moving the objective on the piezostage. A sensitive photomultiplier tube was used to analyse the SHG signal in fast mapping.
Raman characterization of pristine 2H and 1T′ phases. To distinguish the 2H and 1T′ phases of monolayer $MoTe_2$, we measured Raman spectra of exfoliated monolayers from 2H and 1T′ bulky synthetic crystals[35]. For consistency with all other measurements, we kept the temperature at 220 K. In addition, we chose 632.8-nm laser excitation specifically because it shows high Raman intensity for monolayers and could be used for layer identification[36]. In Extended Data Fig. 1, we compare the Raman spectra for each phase. In the measured spectral range, the 2H monolayer exhibits two characteristic Raman peaks, at 171.5 cm^{-1} (A_1') and 236.0 cm^{-1} (E′). By contrast, there is only one dominant peak, at 166.8 cm^{-1} (A_g), in a pristine monolayer 1T′ flake[37,38]. This Raman mode is consistent with the rising new Raman peak (at 167.5 cm^{-1}) that is induced by electrostatic gating. Given the minor Raman shift difference resulting from strain applied by the electrode, we identify the gate-induced new Raman peak as the A_g mode in the 1T′ phase. No Raman features from ionic liquid showed up in this studied range.
Calculations of Raman peaks in constrained 1T′ monolayers. All of our computational work used density functional theory (DFT). All DFT calculations were performed with the Vienna *ab initio* simulation package (VASP)[39], and we used the projected-augmented wave (PAW) method[40,41]. We treated electron exchange and correlation effects with the generalized gradient approximation (GGA) functional of Perdew, Burke and Ernzerhof (PBE)[42]. We used a plane-wave basis set with a kinetic energy cut-off of 350 eV. We sampled the Brillouin zone using an $18 \times 18 \times 1$ Monkhorst–Pack[43] k-point grid. A rectangular unit cell with two formula units of $MoTe_2$ was used. The computational cell is 16 Å along the interlayer direction.

Mechanical constraints on the monolayer are expected to have some effect on the Raman peaks. At zero stress, the 2H phase and 1T′ phase of monolayer $MoTe_2$ have different lattice constants. Therefore, the lattice constants would be expected to change when a transition from the 2H phase to the 1T′ phase occurs at zero stress. However, substrate friction could prevent the lattice constants from changing by fully or partially inhibiting sliding. Therefore, the lattice constants of the electrostatic-doping- induced 1T′ phase could be in between the pristine 1T′ phase lattice constants and the 2H phase lattice constants, depending on the magnitude of the substrate friction. To study this strain effect, we calculated the peak shift of the A_g mode of 1T′ phase monolayer $MoTe_2$ using different lattice constants (a, b), ranging from the pristine 1T′ phase lattice constants ($a^{T'}$, $b^{T'}$) to the 2H phase lattice constants (a^{H}, b^{H}), as follows:

$$\begin{cases} a = a^{T'} + x \bullet (a^{H} - a^{T'}) \\ b = a^{T'} + x \bullet (b^{H} - a^{T'}) \end{cases}$$

$$\begin{cases} x = 0 : a = a^{T'} = 3.452\ \text{Å},\ b = b^{T'} = 6.368\ \text{Å} \\ x = 1 : a = a^{H} = 3.551\ \text{Å},\ b = b^{H} = 6.149\ \text{Å} \end{cases}$$

In Extended Data Fig. 2, the shift in the Raman peak of the A_g mode is shown at different lattice constants. We find that the peak position of the A_g mode of the induced 1T′ phase could be larger than that of the pristine 1T′ phase owing to strain caused by substrate friction. This is consistent with the experimental finding that the A_g mode of the induced 1T′ phase is 167.5 cm^{-1}, and that of the pristine 1T′ phase is 166.8 cm^{-1}.
Raman fitting for a mixture of states. During the phase transition, the sample contains a mixture of 2H and 1T′ states and so the Raman spectra are complex, requiring careful analysis. To fit the mixture and obtain the strength for each mode, we used a Lorentz function[44], $y = y_0 + \frac{2A}{\pi} \times \frac{w}{4(x - x_c)^2 + w^2}$, which peaks at x_c with a width w and an amplitude A; x and y denote the wavenumber and Raman intensity, respectively. The green and blue fitting lines in Extended Data Fig. 3 represent the 2H and 1T′ phases, respectively. Before and after the phase transition, only one phase exists and can be well fitted (Extended Data Fig. 3a, b). Extended Data Fig. 3c shows a typical Raman mixture obtained during the phase transition, for example, at 3.6 V bias. With different characteristic peak positions for the 2H and 1T′ phases, the fitting curves can reveal the weights of the 2H and 1T′ Raman modes.
SHG hysteresis during phase transition. Hysteresis emerges in gate-dependent SHG spectra as well as in Raman spectra. The 2H (or 1T′) phase of monolayer $MoTe_2$ is without (or with) inversion symmetry, leading to the SHG signal being on (or off). Therefore, the SHG signal is expected to disappear and reappear during transition from the 2H to the 1T′ state and vice versa. When changing the gate bias forwards and backwards continuously, we found an SHG hysteresis loop (Extended Data Fig. 4a), which is consistent with the hysteresis seen in Raman spectra (Fig. 2b), having the same width and transition threshold for the same sample. Thus hysteresis is inherent during this phase transition.
Eliminating the effect of molecular movement on hysteresis. To minimize the possibility that hysteresis might result from the slow movement of molecules in the ionic liquid, we extended the stabilization time for each gate in all experiments mentioned above to two minutes[22]. To ensure the validity of this solution, we conducted another SHG measurement on bilayer $MoTe_2$ (Extended Data Fig. 4b); because of the prolonged stabilization time, no hysteresis was observed. The absence of hysteresis in the bilayer is expected because more electrons are required to induce the phase transition in both layers; this finding excludes the possibility that the observed hysteresis in the monolayer originates from the ionic liquid.
Lack of phase transition with doping holes. A positive gate voltage injects electrons into 2H-phase $MoTe_2$; by contrast, a negative gate voltage allows us to study the effects of doping holes (Extended Data Fig. 4c). When holes are added, the SHG signal increases slightly rather than dropping sharply; this small change can be explained by a resonance effect (see below). Both signatures of the 2H-to-1T′ phase transition—the sharp decrease in the SHG signal and the hysteresis—are missing on hole doping. This agrees with the theoretical expectation that the doping requirement for holes is more than twice that for electrons[7,8], and goes beyond the maximum voltage that we could apply (4.5 V). Therefore it is understandable that no phase transition is seen.
First-principle calculations of the 1T′ Raman tensor. We calculated the Raman tensor[45] of the A_g mode of the 1T′ monolayer to be:

$$\begin{bmatrix} \alpha_{xx} & 0 & 0 \\ 0 & \alpha_{yy} & 0 \\ 0 & 0 & 0 \end{bmatrix}$$

where α_{xx}/α_{yy} is 2.3 (details of DFT calculations are given above; α_{xx}/α_{yy} are diagonal tensor elements). The anisotropy of the Raman tensor will lead to polarization dependence of the Raman intensity of the A_g mode. The polarized Raman intensity is proportional to $|\hat{e}_i \bullet R \bullet \hat{e}_s|^2$, where $\hat{e}_i$ and $\hat{e}_s$ are the polarizations of the incident and scattered photons, and R is the Raman tensor for a given mode. In

© 2017 Macmillan Publishers Limited, part of Springer Nature. All rights reserved.

our Raman measurement configuration, the laser excitation is linearly polarized and the polarization can be rotated by a half-wave plate. Meanwhile, there is no selection on scatter polarization. Therefore, the measured Raman intensity is the summation of both parallel and perpendicular scattering components with respect to the incident polarization. Given the calculated Raman tensor for the A_g mode and $\hat{e}_i = (\cos\theta, \sin\theta)$, where the angle θ is measured with respect to the X' axis in the 1T′ phase, the angular Raman intensity is expected to be proportional to $\frac{1}{2}\bullet\left[\left(a_{xx}^2 + a_{yy}^2\right) + \left(a_{xx}^2 - a_{yy}^2\right)\cos 2\theta\right]$. The polarization Raman data in Fig. 3a are well fitted by this formula, confirming the formation of the 1T′ phase under gate control.

Polarized Raman measurement on pristine 1T′ $MoTe_2$. Exfoliated monolayer 1T′ phase $MoTe_2$ showed a notable anisotropic Raman polarization pattern (Extended Data Fig. 5). By rotating the polarization of the excitation laser and collecting Raman scattering, we detected a two-lobe pattern. This unique pattern results from the distorted lattice structure in the 1T′ phase, and is quantitatively consistent with the calculated anisotropic Raman tensor (above), proving that angular polarized Raman spectroscopy is an effective method for characterizing the structure of two-dimensional materials.

Excitonic resonance effect on SHG. We carried out a wavelength scan of SHG intensity before (gate bias 0 V) and after (4.4 V) phase transition (Extended Data Fig. 6). At zero gate bias, we observed a notable resonance at 1,100-nm pumping in phase 2H, attributable to the 1*s* resonance[24]. For the scan wavelength range from 1,020 nm to 1,160 nm, the SHG intensity at 4.4 V is globally more than one order of magnitude lower than that at 0 V. Previous studies showed that gate-bias-induced charging can modify the resonant strength of neutral and charged excitons or even remove excitonic resonance owing to screening of the Coulomb interaction[23,46]. Such a modification may lead to a drop in SHG intensity if the non-linear optical process is assisted mainly by excitonic resonance. For non-resonant excitation, the SHG intensity or absorption profile was almost independent of doping in these reports. However, in monolayer $MoTe_2$ under a high gate bias, we observed a substantial decrease in SHG intensity for both resonant and non-resonant pumping. On the one hand, this observation and the measured SHG hysteresis (Extended Data Fig. 4a) exclude a gate-induced shift in the excitonic resonance peak and a doping-induced modification of absorption strength as the main mechanisms for the drop in intensity. On the other hand, this signature confirms the presence of the 1T′ phase with inversion symmetry. To reduce the effects of excitonic resonance on SHG intensity, we carefully select 1,066 nm as the wavelength for other gate-dependent SHG measurements.

SHG mapping at typical gate bias. We can fit the spatial distribution of the phase-transition threshold (Fig. 4d) from the SHG mapping at each gate bias; examples at typical biases are shown in Extended Data Fig. 7, and show a uniform SHG intensity over the whole flake. A simultaneous dimming in SHG intensity over the whole flake as the gate increases denotes a uniform transition. To study this uniformity of transition quantitatively, we analyse the SHG change at each spatial point through the fitting model discussed below, and plot the threshold in Fig. 4d.

Fitting model for gate-dependent SHG. There are several common features in the gate dependence of the SHG data throughout the flake. First, from 0 V to 2 V, the SHG intensity increases slightly, which we attribute to the shift in the SHG resonance peak of the 2H phase as a function of the doping level. Given that the excitation wavelength is not close to any optical resonance, we assume that the dependence is weak and approximately linear. Second, the SHG decreases gradually from 2 V to 4 V owing to the transition to the 1T′ phase. This transition can be described by the Preisach model[47]: each of the pixels contains many nucleation centres with different transition points. As the literature suggests[48], we assumed that the transition points obey a Gaussian distribution and so the fraction of the 1T′ area is an error function of the gate. Third, the signal finally converges to a non-zero background level. Therefore, we built the following model to describe the gate dependence of SHG: $I = (A + Bx)(1 - \mathrm{erf}(\frac{x - C}{D})) + 0.003$, where A is the SHG intensity at 0 V; Bx is the gate dependence of phase-2H SHG; x represents the gate voltage; C is the centre of the transition voltage; and D is the deviation. A background noise of 0.003 was measured in a clean area without sample and comes from the electronics of the set-up. Figure 4c shows that the model fits the experimental data well.

Analysis of the mechanism of phase transition. *Analysis of doping level assuming a kinetic barrier.* The threshold accumulated carrier density for a typical structural phase transition in monolayer $MoTe_2$ is estimated by measuring the Hall effect. Before making this measurement, we determined the threshold gate voltage for the phase transition in an ionic-liquid-gated device via gate-dependent Raman spectra. The gate-dependent ratio of the 1T′ phase Raman intensity to the whole Raman intensity around 170 cm^{-1} shows a typical hysteresis loop. We determine the threshold gate bias for the phase transition (Extended Data Fig. 8a; red dashed line) to be 3.2 V, fitted from a Preisach model. At this gate bias, we took a Hall measurement under a magnetic field (B) of up to 9 T on the same device with a typical Hall geometry[49]. Extended Data Fig. 8b shows the Hall resistance, R_{xy}, as a function of B at 3.2 V. The Hall resistance curve can be linearly fitted (black dash line) and suggests that the estimated sheet carrier density is $2.2 \times 10^{14}\,cm^{-2}$, which is derived by $n_{2D} = 1/|R_H e|$, $R_H = \frac{R_{xy}(B) - R_{xy}(0)}{B}$, where $R_{xy}(B)$ is the transverse resistance under field B, and $R_{xy}(0)$ is the transverse resistance without field B. This doping level is higher than that predicted theoretically[7] (0.4–$1 \times 10^{14}\,cm^{-2}$). We suspect that this difference results from the presence of kinetic barriers during transition, which are not considered in the theoretical calculation because of computational complicity. Such kinetic barriers lead to the observed hysteresis and set a requirement for a higher doping level to achieve transition.

Analysis of doping level assuming no kinetic barrier. In the theoretical prediction, the energy difference between the 2H and 1T′ states evolves as the carrier density varies[7]. These authors[7] calculated the carrier density needed to drive the 2H-to-1T′ transition assuming that the two phases have the same system energy. As mentioned above, computational complexity prevented the authors from taking the kinetic barrier into account, but we have found experimentally that there is a kinetic barrier and that it results in hysteresis. So, to compare our results with the theoretical results, we need to determine the critical voltage and corresponding carrier density at which the two phases have the same energy. Following a typical method[50], we determined this voltage to be the middle point in the hysteresis loop; it is the average of the voltages at which the 2H-to-1T′ and 1T′-to-2H transitions begin. In the hysteresis loop extracted from gate-dependent Raman spectra (Extended Data Fig. 8c), the starting voltage for the 2H-to-1T′ transition is 2.6 V; that for the 1T′-to-2H transition is 2.2 V. Therefore, the critical voltage is 2.4 V.

We then estimated the corresponding carrier density. Extended Data Fig. 8d shows the Hall resistance, R_{xy}, as a function of the magnetic field, B, at 2.4 V. The Hall resistance curve can be linearly fitted (black dashed line) and suggests the sheet carrier density to be $0.85 \times 10^{14}\,cm^{-2}$. The fitting error for this linear curve is $6 \times 10^{11}\,cm^{-2}$, which is negligible. However, there is an uncertainty ± 0.1 V for the determination of the critical voltage, equivalent to one scanning step used in gate-dependent Raman measurement. This critical voltage of 2.4 ± 0.1 V gives a range for the critical carrier density that is centred at $0.85 \times 10^{14}\,cm^{-2}$ with an uncertainty of $\pm 0.16 \times 10^{14}\,cm^{-2}$, determined by the measured carrier density at adjacent voltages. This carrier range sits within theoretical predictions (0.4–$1 \times 10^{14}\,cm^{-2}$), and this consistency confirms that the mechanism behind our observed 2H-to-1T′ phase transition is electrostatic doping. The low and high ends of the predicted range correspond to conditions of constant stress (where the monolayer is freely suspended) and constant area (where the lattice constant is clamped), respectively[7]. In the actual experimental scenario, monolayers are supported by the substrate with surface friction; we suspect that this friction partially limits the structural relaxation for the monolayer flake. So, it is reasonable that the measured critical carrier density sits between the low and high ends of the predicted values.

Excluding thermal effects during phase transition. To exclude the possibility that a thermally induced phase transition is involved in the Raman measurements, we carried out two control experiments. First, we continuously exposed a monolayer of 2H-phase $MoTe_2$, without gate bias, to a 1 mW μm^{-2} 633-nm laser for 20 hours; this is much longer than the time taken for one run of gate-dependent Raman measurements. We observed neither a new peak nor a shift in the Raman peaks (Extended Data Fig. 9a), confirming that such laser irradiance cannot induce a 2H-to-1T′ phase transition[19]. Second, we applied gate bias: we carried out two full runs of gate-dependent Raman measurements on a sample excited by 633-nm laser with a power of 0.1 mW μm^{-2} or 1 mW μm^{-2}. By analysing the components of the 2H (A_1') and 1T′ (A_g) phases derived from Lorentz fitting, we could visualize the gate-dependent ratios for the Raman intensity of the A_g peak over the overall intensity of the A_1' and A_g peaks for each power condition (as in Fig. 2b). We found that the thresholds and hysteresis loops are the same (Extended Data Fig. 9b). This contradicts the idea of a thermally driven phase transition, in which a power difference of one order of magnitude has a substantial effect on phase transition owing to a change in the local temperature. This power independence of hysteresis characteristics confirms that thermally induced phase transition is negligible.

Data availability. The data that support the findings of this study are available from the corresponding author on reasonable request.

34. Shiogai, J., Ito, Y., Mitsuhashi, T., Nojima, T. & Tsukazaki, A. Electric-field-induced superconductivity in electrochemically etched ultrathin FeSe films on $SrTiO_3$ and MgO. *Nat. Phys.* **12,** 42–46 (2016).
35. Deng, K. *et al.* Experimental observation of topological Fermi arcs in type-II Weyl semimetal $MoTe_2$. *Nat. Phys.* **12,** 1105–1110 (2016).
36. Ruppert, C., Aslan, B. & Heinz, T. F. Optical properties and band gap of single-and few-layer $MoTe_2$ crystals. *Nano Lett* **14,** 6231–6236 (2014).
37. Park, J. C. *et al.* Phase-engineered synthesis of centimeter-scale 1T′- and 2H-molybdenum ditelluride thin films. *ACS Nano* **9,** 6548–6554 (2015).

© 2017 Macmillan Publishers Limited, part of Springer Nature. All rights reserved.

38. Song, Q. *et al.* Anomalous in-plane anisotropic Raman response of monoclinic semimetal 1T′-$MoTe_2$. *Sci. Rep.* **7,** 1758 (2017).
39. Kresse, G. & Furthmüller, J. Efficient iterative schemes for ab initio total-energy calculations using a plane-wave basis set. *Phys. Rev. B* **54,** 11169–11186 (1996).
40. Blöchl, P. E. Projector augmented-wave method. *Phys. Rev. B* **50,** 17953–17979 (1994).
41. Kresse, G. & Joubert, D. From ultrasoft pseudopotentials to the projector augmented-wave method. *Phys. Rev. B* **59,** 1758–1775 (1999).
42. Perdew, J. P., Burke, K. & Ernzerhof, M. Generalized gradient approximation made simple. *Phys. Rev. Lett.* **77,** 3865–3868 (1996).
43. Pack, J. D. & Monkhorst, H. J. Special points for Brillouin-zone integrations. *Phys. Rev. B* **16,** 1748–1749 (1977).
44. Xi, X. *et al.* Strongly enhanced charge-density-wave order in monolayer NbSe2. *Nat. Nanotechnol.* **10,** 765–769 (2015).
45. Fonari, A. & Stauffer, S. vasp_raman.py. https://github.com/raman-sc/VASP/ (2013).
46. Chernikov, A., Ruppert, C., Hill, H. M., Rigosi, A. F. & Heinz, T. F. Population inversion and giant bandgap renormalization in atomically thin WS_2 layers. *Nat. Photon.* **9,** 466–470 (2015).
47. Ramírez, J. G., Sharoni, A., Dubi, Y., Gómez, M. E. & Schuller, I. K. First-order reversal curve measurements of the metal-insulator transition in VO_2: signatures of persistent metallic domains. *Phys. Rev. B* **79,** 235110 (2009).
48. Hadjipanayis, G. C. (ed.) *Magnetic Hysteresis in Novel Magnetic Materials* (Springer, 1997).
49. Shi, W. *et al.* Superconductivity series in transition metal dichalcogenides by ionic gating. *Sci. Rep.* **5,** 12534 (2015).
50. Chandra Shekar, N. V. & Rajan, K. G. Kinetics of pressure induced structural phase transitions—a review. *Bull. Mater. Sci.* **24,** 1–21 (2001).

© 2017 Macmillan Publishers Limited, part of Springer Nature. All rights reserved.

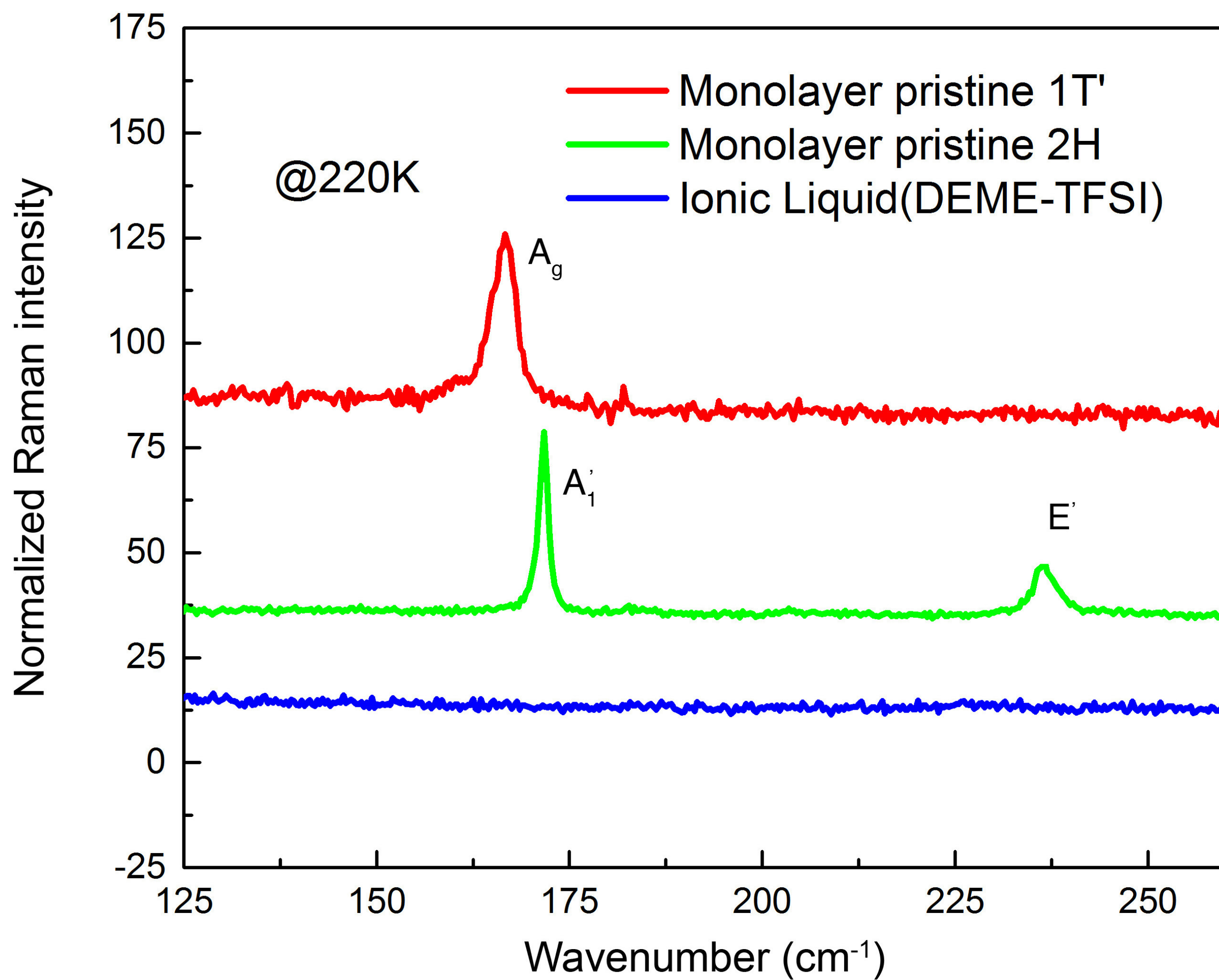

Extended Data Figure 1 | Raman features of pristine 2H-and 1T′-phase monolayer $MoTe_2$ at 220 K. Raman spectra for the 2H and 1T′ phases of monolayer $MoTe_2$ are plotted in green and red, respectively. The Raman modes at 171.5 cm^{-1} and 236 cm^{-1} are the A_1' and E′ oscillation modes, belonging to the 2H phase. Excited by the same wavelength (632.8 nm), the 1T′ monolayer has just one dominant mode, at 166.8 cm^{-1}. The blue curve, from bare ionic liquid, shows no Raman modes and so acts as a clear and flat background in all Raman measurements.

© 2017 Macmillan Publishers Limited, part of Springer Nature. All rights reserved.

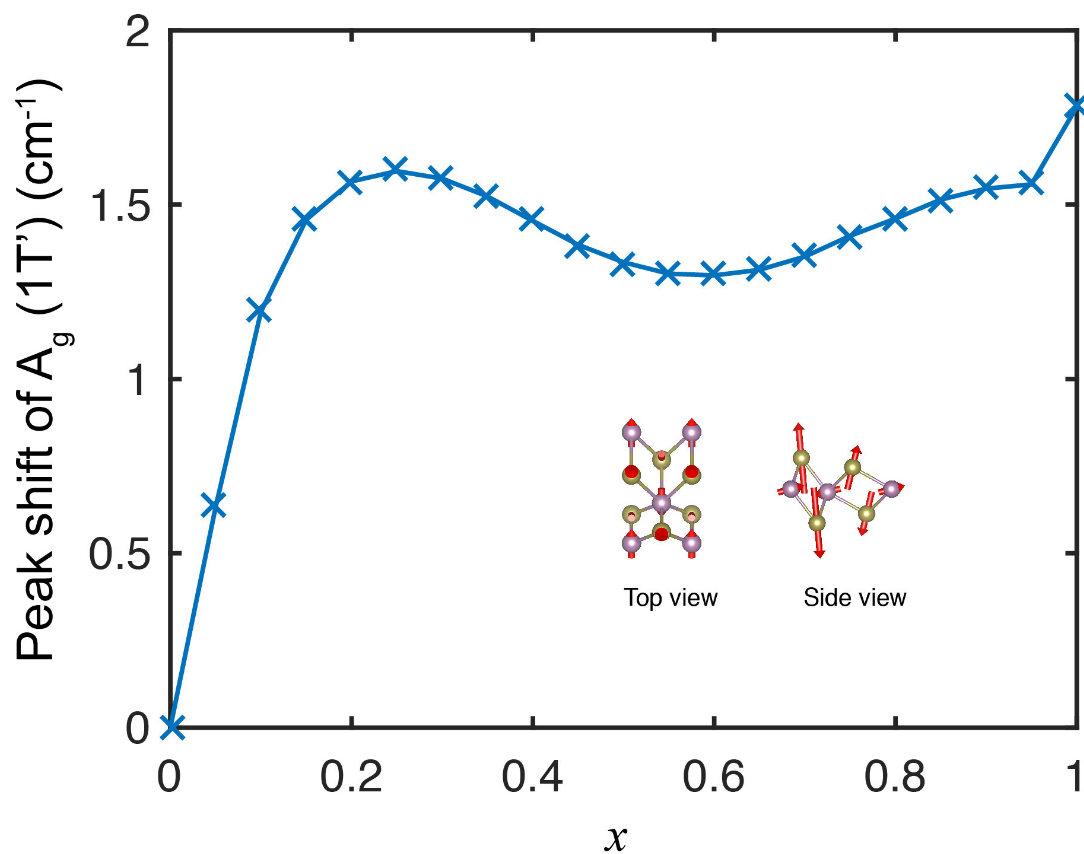

Extended Data Figure 2 | Calculated shift in the Raman peak of the A_g mode of the 1T′-phase $MoTe_2$ monolayer owing to strain. The lattice constants range from ($a^{T'}$ $b^{T'}$) at $x = 0$ to (a^{H}, b^{H}) at $x = 1$. All lattice constants can be found in the Methods. Inset, top and side views of the atomic displacement pattern of the A_g mode. The magnitude of the displacements is proportional to the length of the red arrows. Purple and yellow spheres denote molybdenum and tellurium atoms, respectively.

© 2017 Macmillan Publishers Limited, part of Springer Nature. All rights reserved.

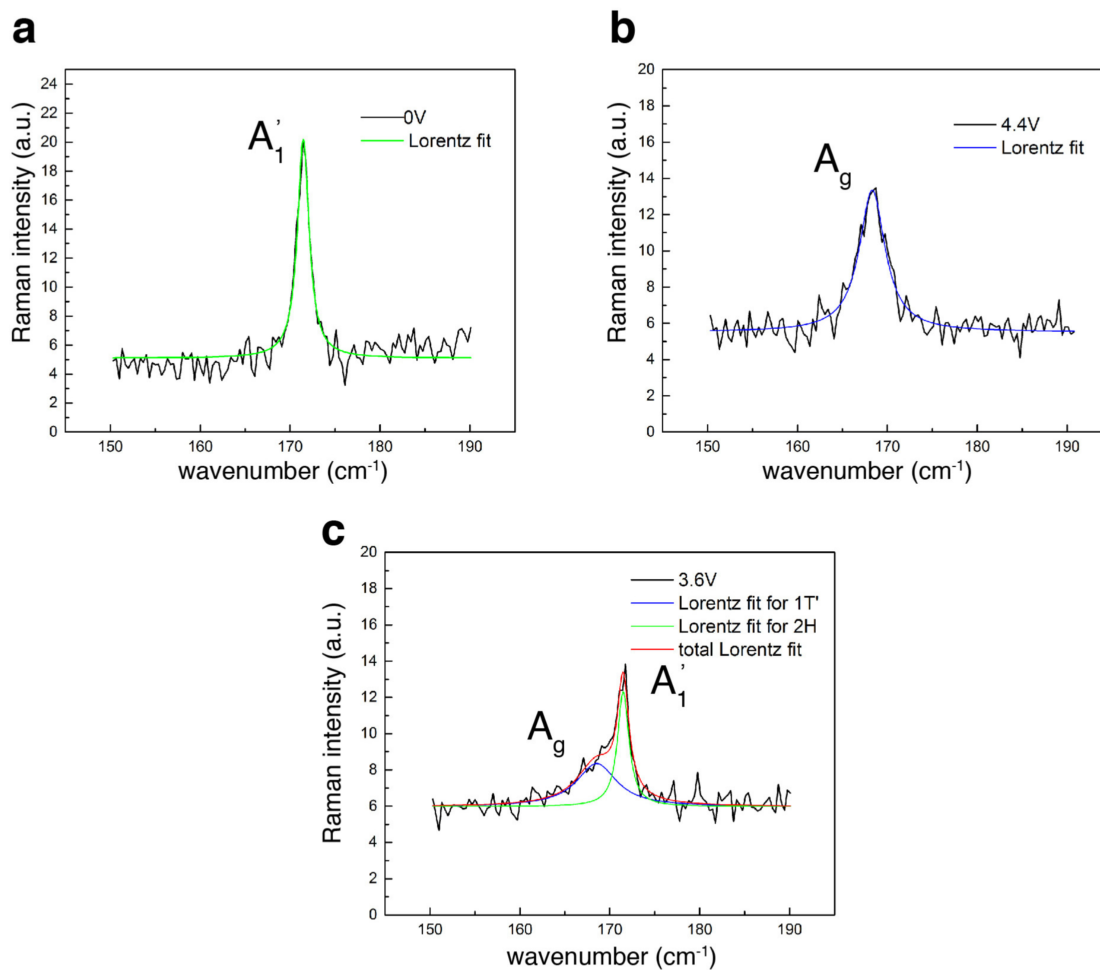

Extended Data Figure 3 | Fitting of the Lorentz function for Raman spectra at different biases. **a**, **b**, Raman spectra at 0 V and 4.4 V are well fitted by only one Lorentz function, representing a single Raman mode (A_1' in the 2H phase, and A_g in the 1T′ phase). **c**, A typical Raman spectrum taken during transition from one phase to another (for example, at a bias of 3.6 V) is well fitted by two Lorentz functions, centred at A_1' and A_g.

© 2017 Macmillan Publishers Limited, part of Springer Nature. All rights reserved.

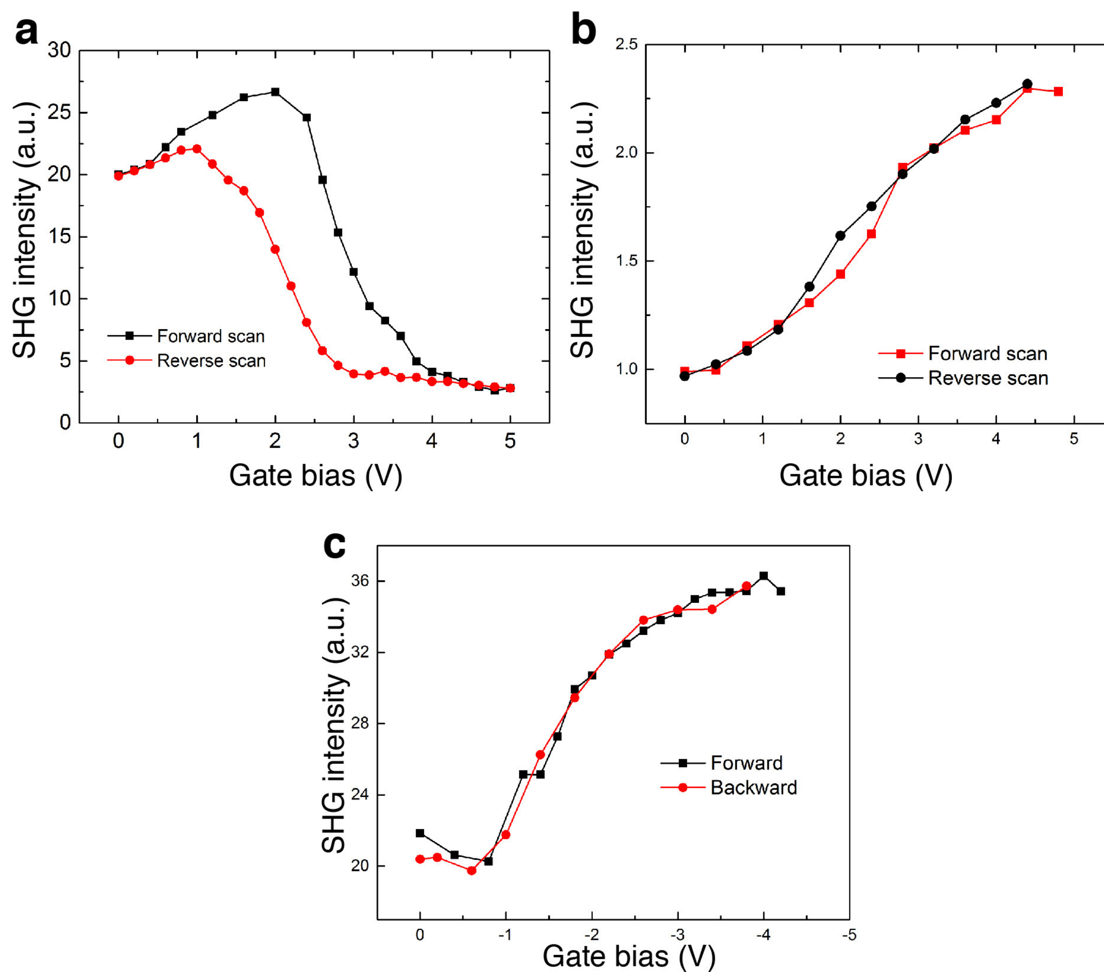

Extended Data Figure 4 | Gate-dependent SHG spectroscopy of monolayer and bilayer 2H $MoTe_2$. **a**, The SHG intensity of monolayer $MoTe_2$ displays notable hysteresis during forward and backward alteration of the positive top gate (thereby altering the doping of the sample with electrons). The large variation in SHG intensity results mainly from a change in inversion symmetry during phase transition. **b**, The SHG intensity of a bilayer sample shows no hysteresis under sweeping of the top gate bias. **c**, Doping with holes (that is, by applying a negative top gate voltage) into 2H monolayer $MoTe_2$ slightly increases the SHG intensity by 1.5 times; a reserve gate sweep shows no hysteresis.

© 2017 Macmillan Publishers Limited, part of Springer Nature. All rights reserved.

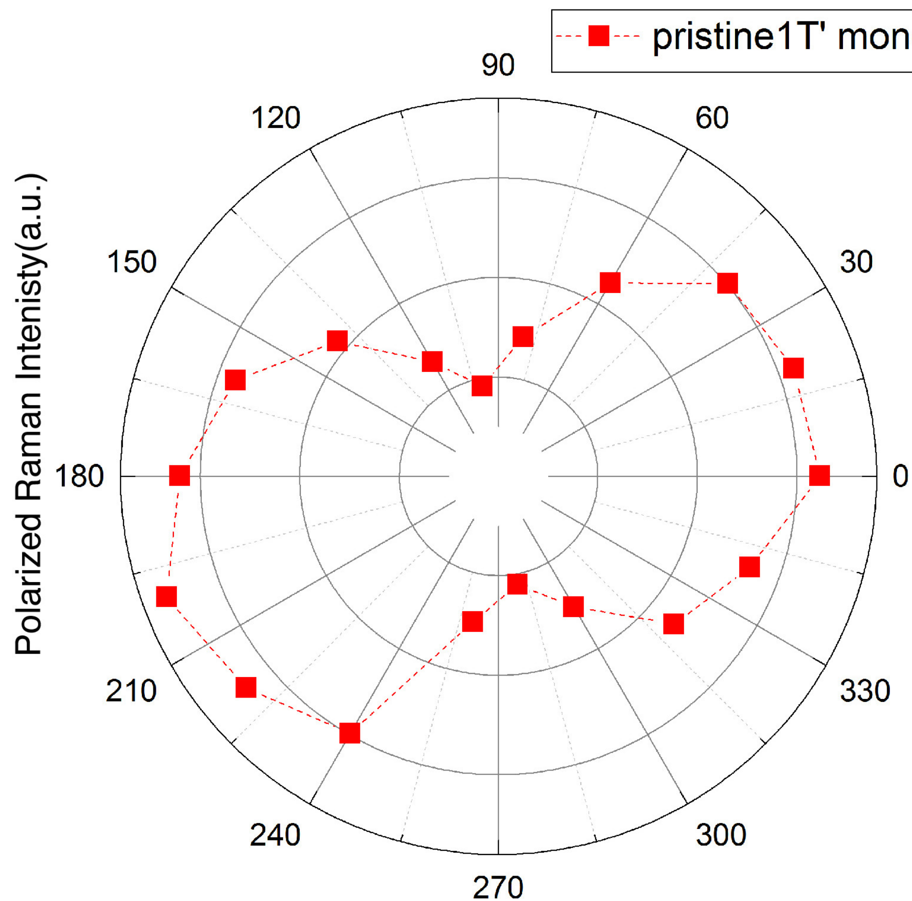

Extended Data Figure 5 | Angular polarized Raman (A_g mode) pattern on an exfoliated 1T′-phase $MoTe_2$ monolayer. The position of zero degrees is arbitrary. By rotating the polarization of the excitation laser, we detected a twofold pattern, verifying the anisotropic *xx* and *yy* components in the A_g Raman tensor.

© 2017 Macmillan Publishers Limited, part of Springer Nature. All rights reserved.

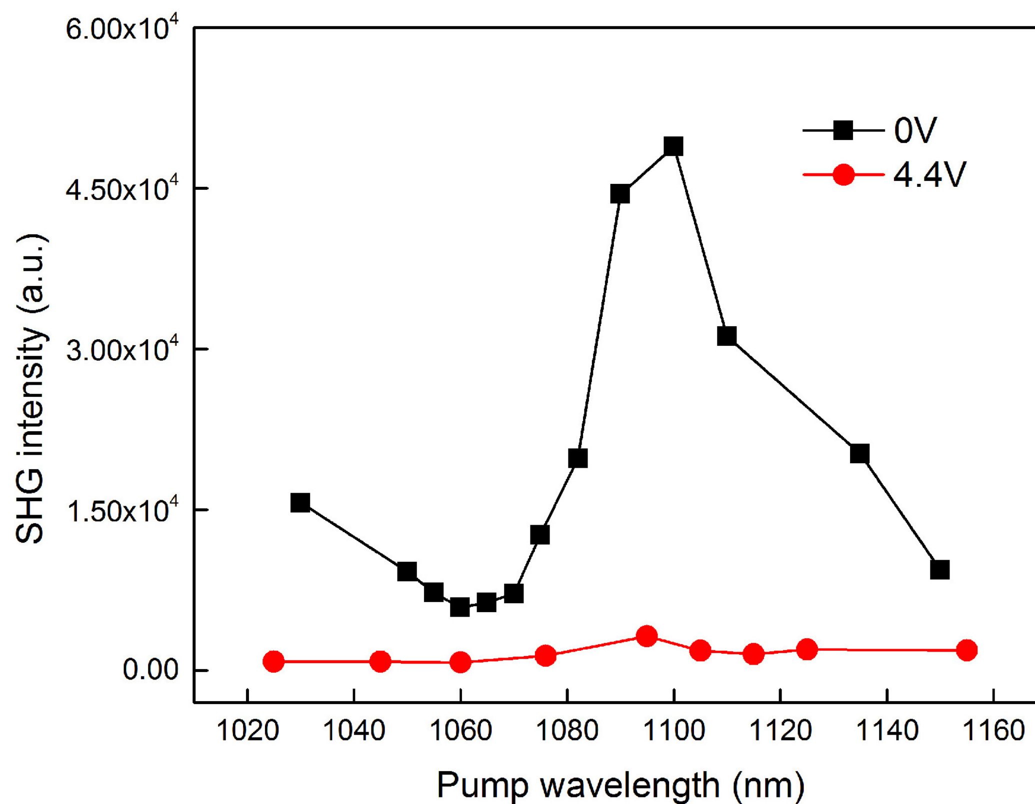

Extended Data Figure 6 | SHG intensity versus excitation energy before and after phase transition. At a gate bias of 0 V and a pump wavelength of 1,100 nm, a notable excitonic resonance is observed in a 2H-phase $MoTe_2$ monolayer. At the same pump power but a bias of 4.4 V, the SHG intensity drops by more than one order of magnitude over the entire excitation spectrum range. The incident excitation power for each wavelength was fixed at the same level. The sample was kept at a temperature of 220 K during the measurements.

© 2017 Macmillan Publishers Limited, part of Springer Nature. All rights reserved.

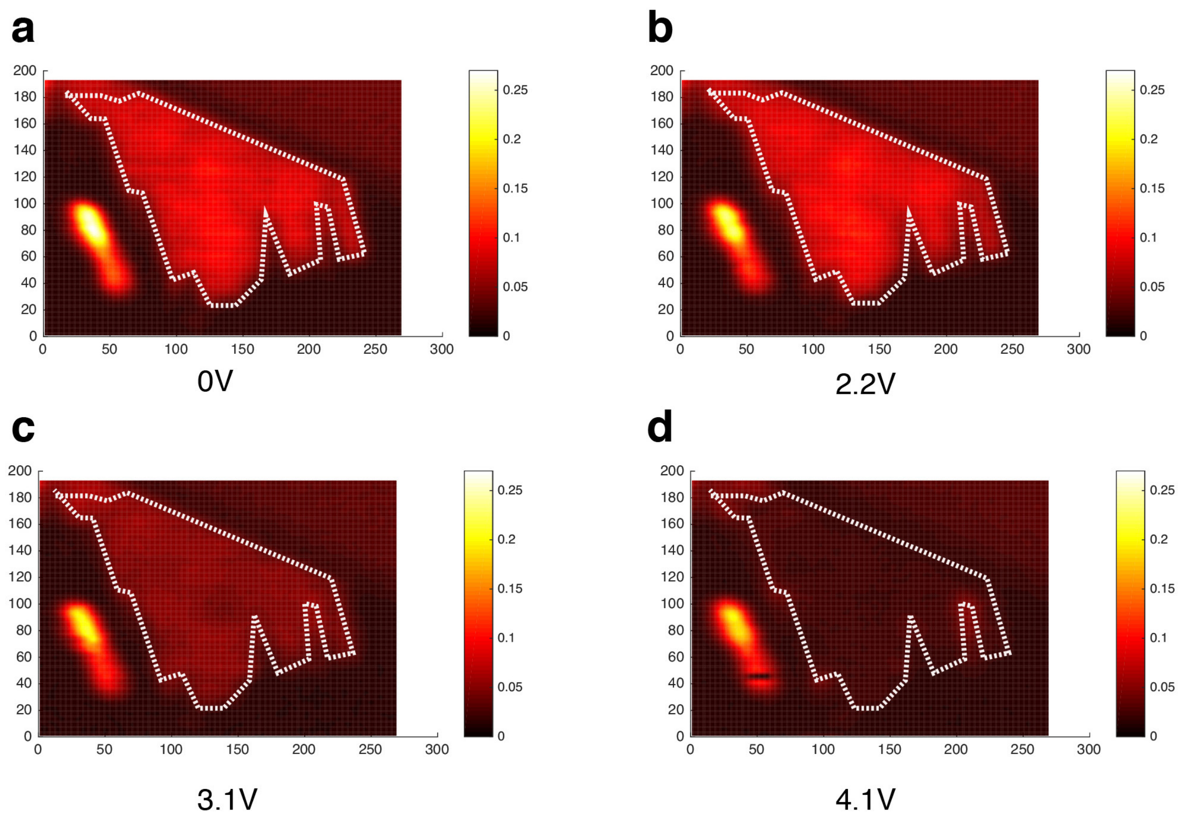

Extended Data Figure 7 | SHG mapping at several typical voltage biases. a–d, These biases correspond to before (0 V and 2.2 V; **a**, **b**), during (3.1 V; **c**) and after (4.1 V; **d**) phase transition.

© 2017 Macmillan Publishers Limited, part of Springer Nature. All rights reserved.

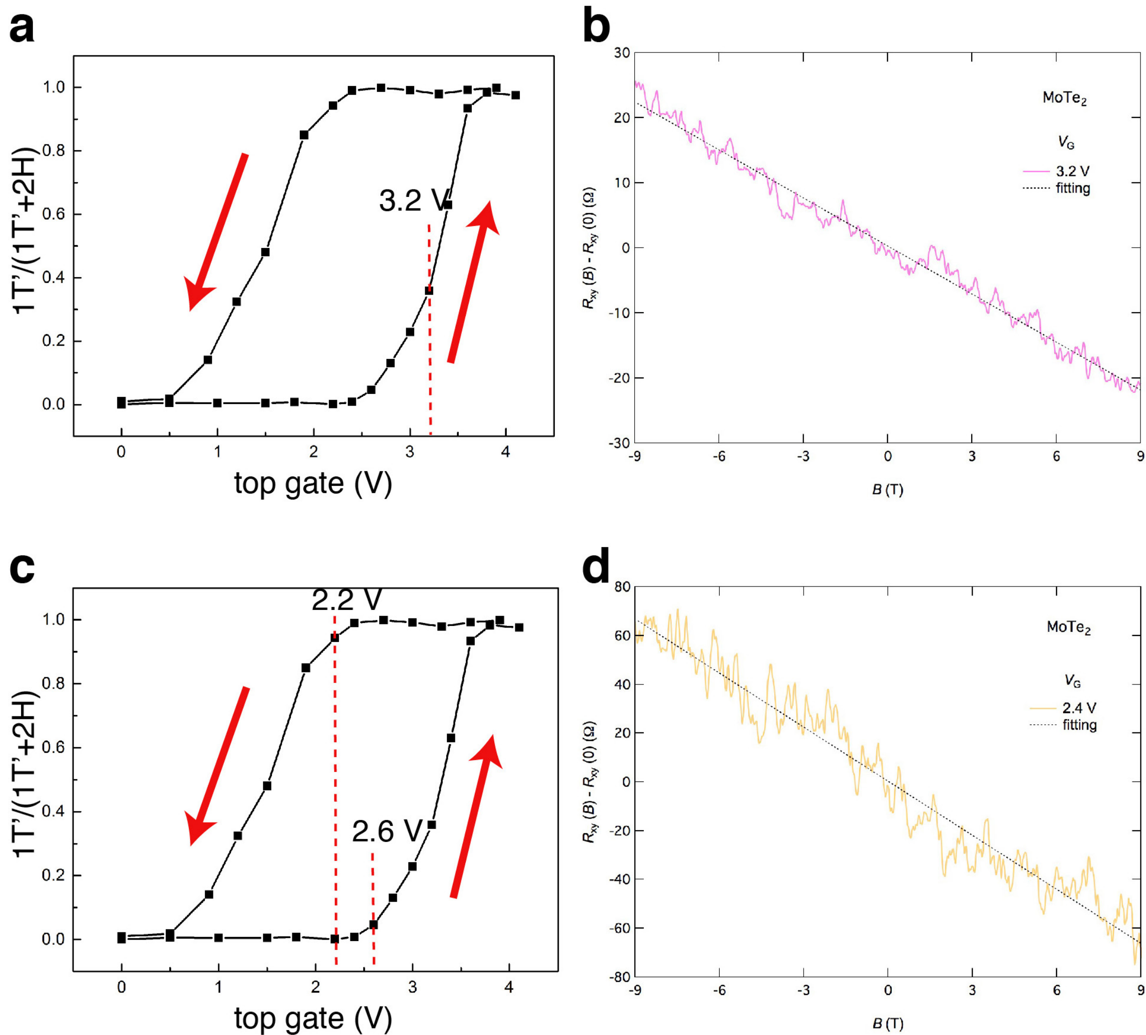

Extended Data Figure 8 | Analysis of the mechanism of phase transition from 2H to 1T′ by the Hall effect. a, **c**, Gate-dependent Raman intensity ratio. The ratio (1T′/1T′ + 2H)) is extracted from Lorentz fitting of Raman spectroscopy at each gate (as in Fig. 2b). Red arrows show forward and backward gate sweeping. From **a**, we determine the threshold for transition from phase 2H to 1T′ to be 3.2 V (red dashed line) on the basis of fitting with the Preisach model. The corresponding carrier density at this threshold is higher than that predicted theoretically[7], perhaps because of the presence of kinetic barriers during transition, which were not considered in the theoretical calculation. In order to compare with the predicted critical doping level, where the two phases are energetically degenerate, we determined the corresponding critical voltage in **c**, following a typical method[50]. The red dashed lines indicate that transition from phase 2H to 1T′ occurred at a bias of 2.6 V while the reverse process began at 2.2 V. The average (2.4 V) refers to the critical voltage at which the two phases are energetically degenerate. **b**, **d**, The Hall resistance $[R_{xy} - R_{xy}(0)]$ for the same sample at 3.2 V (**b**) and 2.4 V (**d**), as a function of the magnetic field, B. Here R_{xy} is the transverse resistance under the magnetic field while $R_{xy}(0)$ is the transverse resistance without magnetic field. The slopes of their linear fittings (dashed lines) give the corresponding carrier densities to be 2.2×10^{14} cm^{-2} and 8.5×10^{13} cm^{-2}, respectively. The latter, which excludes the kinetic barrier, matches the carrier range that is predicted[7] to drive this phase transition (0.4–1×10^{14} cm^{-2}).

© 2017 Macmillan Publishers Limited, part of Springer Nature. All rights reserved.

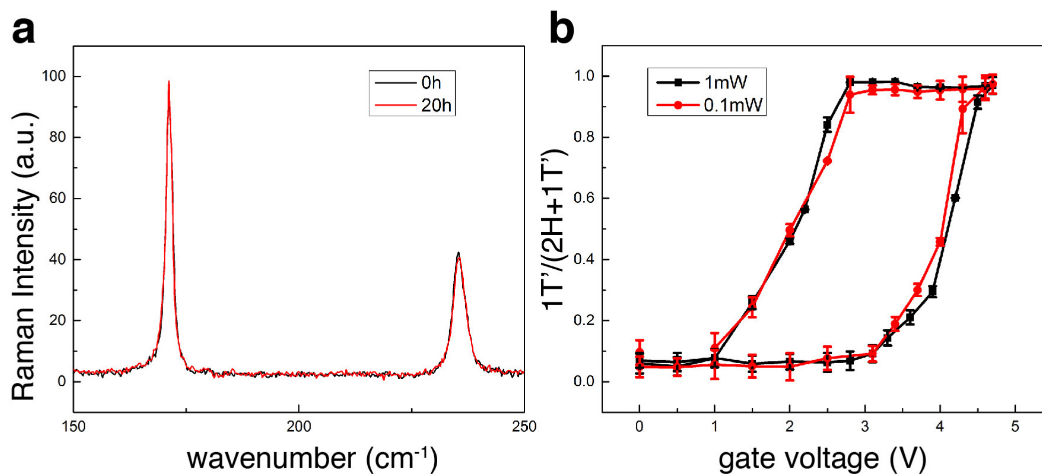

Extended Data Figure 9 | Evidence that the phase transition is not thermally driven during Raman measurements. a, Raman spectra of monolayer 2H $MoTe_2$ before and after exposure to a 1 mW μm^{-2}, 633-nm laser for 20 hours. A shift in neither peak intensity nor peak position is observed. **b**, Gate-dependent Raman intensity ratio (1T′/(2H + 1T′)) under different laser-power excitations: 1 mW μm^{-2} or 0.1 mW μm^{-2}. At each gate voltage, the intensity for the 2H phase (or 1T′ phase) Raman mode A_1 (or A_g) was extracted by Lorentz fitting of the Raman mixture in the range 160–180 cm^{-1}. The error bars represent standard errors propagated from the fitting parameters. Given that the thresholds and hysteresis loops are the same at both powers, the transition between the 2H and the 1T′ phase must be independent of laser power and is determined purely by the electrostatic doping level rather than by a thermal effect. All experiments were conducted in a vacuum of 2×10^{-6} torr and at a temperature of 220 K.

© 2017 Macmillan Publishers Limited, part of Springer Nature. All rights reserved.